



**HAL**  
open science

# Effect of laser beam incidence angle on the thermoelastic generation in semi-transparent materials

Samuel Raetz, Thomas Dehoux, Bertrand Audoin

## ► To cite this version:

Samuel Raetz, Thomas Dehoux, Bertrand Audoin. Effect of laser beam incidence angle on the thermoelastic generation in semi-transparent materials. *Journal of the Acoustical Society of America*, 2011, 130 (6), pp.3691 - 3697. 10.1121/1.3658384 . hal-01889416

**HAL Id: hal-01889416**

**<https://univ-lemans.hal.science/hal-01889416>**

Submitted on 9 Oct 2018

**HAL** is a multi-disciplinary open access archive for the deposit and dissemination of scientific research documents, whether they are published or not. The documents may come from teaching and research institutions in France or abroad, or from public or private research centers.

L'archive ouverte pluridisciplinaire **HAL**, est destinée au dépôt et à la diffusion de documents scientifiques de niveau recherche, publiés ou non, émanant des établissements d'enseignement et de recherche français ou étrangers, des laboratoires publics ou privés.

# Effect of laser beam incidence angle on the thermoelastic generation in semi-transparent materials

Samuel Raetz, Thomas Dehoux, and Bertrand Audoin<sup>a)</sup>

*Université de Bordeaux, UMR CNRS 5295, Institut de Mécanique et d'Ingénierie de Bordeaux,  
Département d'Acoustique Physique, 33405 Talence, France*

(Received 4 April 2011; accepted 5 October 2011)

When a laser beam is absorbed in a semi-transparent material, a volume acoustic source is created owing to penetration of the laser beam inside the material and to thermoelastic transduction. Many experimental and theoretical studies have been conducted to better understand this ultrasound generation process with normal laser light incidence on the material surface. The purpose of this paper is to analyze the effects of the asymmetry caused by oblique incidence of a laser line source on the generation of acoustic waves in semi-transparent isotropic materials. Experiments on a glass plate demonstrate that such an obliquely incident laser light strongly affects bulk acoustic waves generation. Compressional and shear waves are enhanced and the loss of symmetry of the acoustic source causes asymmetrical behavior of the acoustic waves. Surprisingly, compressional-wave amplitude decreases whereas shear-wave amplitude increases in the region where the electromagnetic energy is refracted. This feature is explained by semi-analytical calculations. © 2011 Acoustical Society of America. [DOI: 10.1121/1.3658384]

PACS number(s): 43.35.Sx, 43.38.Zp, 43.35.Cg [JDM]

Pages: 3691–3697

## I. INTRODUCTION

The idea of producing sound with light drawn up in 1880<sup>1</sup> has showed a renewed interest with the emergence of lasers in the early 1960s.<sup>2</sup> Nowadays, the broad range of laser sources in terms of wavelength, peak power, repetition rate, and pulse duration provides a wide set of possible acoustic sources. Following the first quantitative approaches,<sup>3</sup> more detailed investigations have been undertaken to characterize more precisely the laser source. Theoretical and experimental aspects of the generation mechanism have been extensively studied.<sup>4</sup> Effects of the optical penetration of the source,<sup>5</sup> of the thermal diffusion,<sup>6</sup> or of diffraction<sup>7</sup> on acoustic wave generation are well-known. A laser beam focused to a point is usually used for most practical applications. However, it has been pointed out that the use of a laser line source, rather than a point, could enhance wave directivity<sup>8</sup> or increase signal-to-noise ratio.<sup>9</sup> In addition, considering a laser line source eliminates some mathematical complexity in the modeling owing to the symmetry of the source. The first model involving a laser line source was developed to obtain directivity patterns of laser-generated compressional and shear waves.<sup>10</sup> All the modeling and experiments above-mentioned considered a normal incidence of the laser beam illuminating the sample.

Due to the non-contact feature of the technique and to the broad range of frequencies generated, applications to nondestructive material characterization using bulk, surface or guided waves<sup>11,12</sup> are very attractive. Evaluation of physical properties such as shear or tensile stiffness coefficients of an elastic medium can be carried out. To obtain the shear stiffness coefficients, it is mandatory to generate both compressional and shear waves. When the laser spot width at the

sample surface, i.e., the opto-acoustic source width, is small with respect to the generated wavelength, acoustic scattering occurs and yields to the generation of both compressional and shear waves.<sup>13,14</sup> For materials where the optical penetration is small, typically in the nm range for metals, wavelength larger than the opto-acoustic source width can be obtained with ns pulse duration or longer. In the reverse case, contribution of laser heating below the surface must be accounted for. In an infinite medium, the transient laser heating yields a thermal source of expansion that cannot generate shear waves. When this source lies below the surface of a half space mode conversion of the laser-generated compressional waves obliquely incident on the surface contributes to shear-wave generation. Sharp focusing of laser has been demonstrated to create diffracting shear waves with a wide wave-vector spectrum in the GHz frequency range using fs laser pulses.<sup>15</sup> It was shown recently that a laser-induced grating could also serve selecting some of the so-generated oblique shear-wave vectors.<sup>16</sup> In the case of wider sources, where the generated compressional waves are normally incident on the surface, asymmetric boundary conditions can be used to create shear acoustic waves. For example mode-conversion at an isotropic-anisotropic interface<sup>17</sup> or generation of plane shear waves by laser heating of an anisotropic medium<sup>18</sup> can be used.

In millimetric absorbing plates illuminated with a focused laser beam, typically with nanosecond pulse duration and focal spot of tens of microns, shear acoustic waves are diffracted from the source. The loss of symmetry of the thermoelastic volume source could help enhancing and controlling shear-wave generation. The purpose of this paper is to analyze the effects on acoustic waves of the asymmetry caused by oblique incidence of a laser line source focused on isotropic plates. Section II presents a qualitative description of the oblique laser incidence influence on the laser-generated acoustic waves.

<sup>a)</sup>Author to whom correspondence should be addressed. Electronic mail: bertrand.audoin@u-bordeaux1.fr

Acoustic diffraction from an asymmetric thermoelastic source is modeled with a semi-analytical approach using a spatiotemporal Fourier transform. In Sec. III we will demonstrate both theoretically and experimentally that such an obliquely incident source strongly affects bulk waves generation in a glass plate. Effects on the shape and on the amplitude of the compressional and shear waves will be analyzed.

## II. MODELING OF OBLIQUE THERMOELASTIC GENERATION

The sample is an isotropic parallel-sided plate made of colored glass of thickness  $h$ . It is obliquely illuminated by a line-focused laser beam. Let  $\mathbf{x}_1$  be the direction normal to the illuminated surface and  $\theta_i$  the angle of incidence formed by  $\mathbf{x}_1$  and the incident optical wave vector  $\mathbf{k}_i$  [see Fig. 1(a)].  $\mathbf{x}_2$  and  $\mathbf{x}_3$  are completing the Euclidian base, and  $\mathbf{x}_3$  denotes the direction of the laser line source. The lateral size  $a$  of the laser beam along axis  $\mathbf{x}_2$  is the full width at half maximum (FWHM) of the Gaussian distribution of the laser intensity. Since the extension along  $\mathbf{x}_3$  of the laser line source is by hundred times larger than  $a$ , the problem is two-dimensional in the plane normal to the laser line direction  $\mathbf{x}_3$ .

The depth at which a laser beam penetrates into a material depends on the wavelength of the laser light and on the nature of the material itself. The transmitted beam location also depends on the laser beam path after its refraction upon transmission through the surface of the sample. The material is heated within the volume defined by the penetration depth  $\xi$  and the area of the free surface illuminated by the laser beam, depending on  $a$ . This local rise of temperature creates a finite volume source of expansion and compressional acoustic waves are thereby generated. Considering a laser delivering nanosecond pulses, the width of the laser line on the surface is usually about a few tens of microns. In experiments involving nanosecond laser pulses, the characteristic frequency of the laser-generated acoustic waves is typically of the order of the inverse of the laser pulse duration  $\tau_L$ . However, if  $\xi$  is much larger than the propagating distance of the compressional waves of velocity  $V_C$  during  $\tau_L$ ,  $\xi \gg \tau_L V_C$ , the characteristic frequency of laser-generated acoustic waves will be related to  $\xi$  rather than  $\tau_L$ .<sup>19</sup> The glass material under the scope of this paper satisfies this condition and the characteristic angular frequency is thus  $\omega_c = 2\pi V_C / \xi$ . A limiting condition for the diffraction of compressional and shear acoustic waves to occur, neglecting diffusion, is that

the lateral width of the acoustic source  $a$  be such that  $k_{2S} a < 1$ , where  $k_{2S}$  denotes the wave number of the shear mode along the interface.<sup>20</sup> This condition imposes that  $\xi > a$  for shear acoustic waves to be diffracted by the source.

To analyze the propagation of the compressional and shear acoustic waves versus the angle of incidence  $\theta_i$ , a two-dimensional semi-analytical model is presented. The calculation scheme to compute the solution of the wave equation is based on that detailed in Ref. 20. Let us briefly describe this model.

The laser generation of ultrasound is modeled with the partially coupled Fourier heat diffusion equation and elastic wave equation. Thermal heat diffusion is neglected since the time scale of the diffusion is much larger than that of wave propagation. Thus, the heat equation reduces to a simple form:

$$\rho C_p \frac{\partial T}{\partial t}(x_1, x_2, t) = Q(x_1, x_2, t), \quad (1)$$

where  $\rho$ ,  $C_p$ ,  $T$ , and  $Q$  denote the density, the specific heat, the temperature, and the power density absorbed by the sample, respectively. The wave equation with an internal force resulting from the localized heating by the laser light is written as:

$$\nabla \cdot ([C] : \nabla \mathbf{u}) - \rho \frac{\partial^2 \mathbf{u}}{\partial t^2} = [C] : [\alpha] \nabla T, \quad (2)$$

where  $\mathbf{u}$ ,  $[C]$ , and  $[\alpha]$  stand for the displacement vector, the stiffness tensor, and the thermal dilatation tensor, respectively. For given boundary conditions, the solution of the wave equation is calculated analytically using a double Fourier transform in time  $t$  and space  $x_2$ . The corresponding dual Fourier variables are the pulsation  $\omega$  and the component  $k_2$  of the acoustic wave vector  $\mathbf{k}$ .

The change in the source term  $Q$  of the heat equation caused by the oblique incidence of the laser beam is now detailed. The incident laser beam is first modeled as a monochromatic electromagnetic plane wave of angular frequency  $\omega_{\text{opt}}$ . The incident electric field  $\mathbf{E}_i$  is polarized in the plane  $(\mathbf{x}_1, \mathbf{x}_2)$ :

$$\mathbf{E}_i = A_{\parallel} (\sin \theta_i \mathbf{x}_1 - \cos \theta_i \mathbf{x}_2) e^{-j(\omega_{\text{opt}} t - \mathbf{k}_i \mathbf{r})}, \quad (3)$$

with  $\mathbf{k}_i = k_i (\cos \theta_i \mathbf{x}_1 + \sin \theta_i \mathbf{x}_2)$ .  $t$ ,  $\mathbf{r}$ , and  $A_{\parallel}$  are the time, position vector, and the amplitude of  $\mathbf{E}_i$ , respectively. The optical reflection of the laser beam at the second interface of the sample ( $x_1 = h$ ) is not considered since the optical penetration depth is less than the thickness of the sample. The absorption of the transmitted wave in the material is modeled by a complex optical wave vector  $\mathbf{k}_t^*$ . Optical phase continuity at the illuminated interface imposes that  $\mathbf{k}_t^* \cdot \mathbf{x}_2$  is real. The index of refraction  $n^* = n + j\kappa$  is complex in the sample and the law of refraction  $\sin \theta_t = n^* \sin \theta_i$  thus implies that the angle of refraction  $\theta_t$  is complex too.

The local law of conservation of the electromagnetic energy relates the divergence of the optical Poynting vector to the electromagnetic power density. It leads to the following

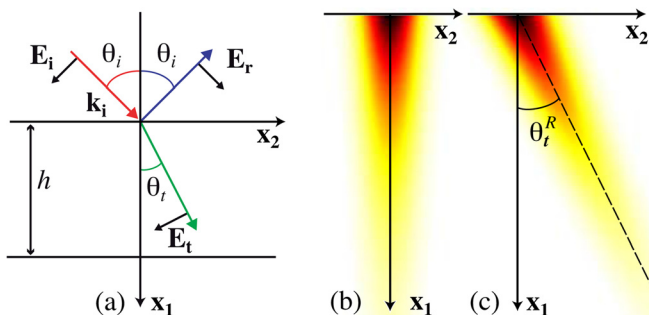


FIG. 1. (Color online) (a) Geometry of the problem. Initial power density calculated for (b)  $\theta_i = 0^\circ$  and (c)  $\theta_i = 45^\circ$ .

expression of the power density for the electromagnetic plane wave considered:

$$Q(x_1) = \beta(\theta_i)K(\theta_i)I_0e^{-\beta(\theta_i)x_1} \quad \forall x_1 \geq 0, \quad (4)$$

$\beta(\theta_i) = 2\text{Im}(k_t^* \cos \theta_i)$  is the inverse of the optical skin depth  $\xi(\theta_i)$ , increasing with  $\theta_i$ .  $I_0$  is the incident intensity of the laser beam.  $K$  is defined as  $K(\theta_i) = \text{Re}(\overline{n^*} \cos \theta_i) |\Gamma^*(\theta_i)|^2$  with  $\overline{n^*}$  the complex conjugate of  $n^*$  and  $\Gamma^*(\theta_i)$  the complex optical transmission coefficient in amplitude through the air-solid interface.

To model a Gaussian incident beam, the power density expressed in Eq. (4) must be modified. The following formalism is based on the assumption that the power density retains its lateral Gaussian profile upon oblique transmission through the interface of the absorbing medium. The validity of this assumption is discussed in Sec. III of the paper. The source term  $Q$  in Eq. (2) is thus:

$$Q(x_1, x_2, t) = \beta(\theta_i)K(\theta_i)I_0e^{-\beta(\theta_i)x_1} \times g(x_1, x_2)f(t) \quad \forall x_1 \geq 0, \quad (5)$$

where  $K$  is modified compared to Eq. (4) to account for Gaussian beam transmission.<sup>21</sup> Function  $f$  stands for the normalized Gaussian time distribution of intensity. Function  $g$  stands for the normalized Gaussian lateral distribution of intensity:

$$g(x_1, x_2) = G(-x_1 \sin \theta_t^R + x_2 \cos \theta_t^R), \quad (6)$$

where  $\theta_t^R = \arcsin(\sin \theta_i/n)$  is the refraction angle calculated from the real part of the refraction index  $n$ . For a non-zero incidence angle, the lateral Gaussian distribution depends on both space variables  $x_1$  and  $x_2$ . Upon normal incidence, the dependency on  $x_1$  vanishes.  $G$  is a Gaussian function defined as:

$$G(y) = \frac{2}{a} \sqrt{\frac{\ln 2}{\pi}} e^{-4 \ln 2 y^2 / a^2}. \quad (7)$$

Thus, the spatial Fourier transform of  $g$ , denoted by  $\tilde{g}$ , is merely:

$$\tilde{g}(x_1, k_2) = \tilde{G}\left(\frac{k_2}{\cos \theta_t^R}\right) \frac{e^{jk_2 x_1 \tan \theta_t^R}}{|\cos \theta_t^R|}, \quad (8)$$

where  $\tilde{G}(k_2/\cos \theta_t^R)$  is also a Gaussian function of  $k_2$  and  $\exp(jk_2 x_1 \tan \theta_t^R)/|\cos \theta_t^R|$  is the spatial Fourier transform of the delta function  $\delta(-x_1 \cos \theta_t^R + x_2 \sin \theta_t^R)$ . In the above notation and in the remainder, the grapheme tilde denotes the spatial Fourier transform on  $x_2$  only. The localization of the source along the refraction direction defined by equation  $x_2 = x_1 \tan \theta_t^R$  is well described by this modeling. Power density mappings at  $t=0$  are shown in Fig. 1 for a pulse duration of 8 ns and a FWHM of 0.1 mm. Figures 1(b) and 1(c) show results for a normal incidence configuration and for an oblique incidence configuration with  $\theta_i = 45^\circ$  corresponding to  $\theta_t^R \sim 29^\circ$  (in the remainder, only  $\theta_i = 45^\circ$  is considered),

respectively. When  $\theta_i = 45^\circ$  the location of the source is along the refracted direction and is no longer symmetrical with respect to axis  $\mathbf{x}_1$ . This loss of symmetry of the source caused by the oblique incidence is the origin of the photoacoustic effects discussed in this paper.

Let us now consider the variation of the temperature gradient  $\nabla T$  since it contains the space dependency of the source term in the wave equation [Eq. (2)]. The initial amplitude of the spatial Fourier transform of each projection  $\tilde{\nabla T} \cdot \mathbf{x}_p$  of  $\nabla T$  in the direction  $p = \{1, 2\}$  is calculated for  $x_1 = 0$ . Quantities  $\Lambda_p(k_2, \theta_i) = |\tilde{\nabla T} \cdot \mathbf{x}_p / \beta K I_0|_{x_1=0, \theta=\theta_i}$  are plotted in Figs. 2(a) and 2(b) versus  $k_2$  for  $\theta_i = 0^\circ$  and for  $\theta_i = 45^\circ$ . The denominator in  $\Lambda_p$  compensates for changes in the absorbed power due to incidence. As mentioned previously, the characteristic angular frequency  $\omega_c(\theta_i) = 2\pi\beta(\theta_i)V_C$  of the compressional waves of velocity  $V_C$  is imposed by the inverse of the optical skin depth  $\beta(\theta_i)$ . The characteristic wavenumber is then defined by  $k_c(\theta_i) = \omega_c(\theta_i)/V_C$ .

We compare both incidence configurations  $\theta_i = 0^\circ$  and  $\theta_i = 45^\circ$  at the same characteristic pulsation  $\omega_c$  ( $\theta_i = 0^\circ$ ).  $\omega_c$  increases with  $\theta_i$  owing to its dependency on the angle of incidence through  $\beta(\theta_i)$ .  $k_c(\theta_i)$  thus increases with increasing incidence.

The vertical lines in Figs. 2(a) and 2(b) denote the wavenumber threshold  $k_2^{\text{lim}} = \omega_c/V_S$  beyond which generated shear waves of angular frequency  $\omega_c$  and velocity  $V_S$  are evanescent. Only the generation of propagating shear waves corresponding to  $k_2 \in [0; k_2^{\text{lim}}]$  is discussed in the following. Figure 2(a) shows that the gradient projection on axis  $\mathbf{x}_1$  is greatly enhanced for  $\theta_i = 45^\circ$  compared to  $\theta_i = 0^\circ$ . To discuss this result, consider the solution  $\tilde{T}$  of Eq. (1) in the Fourier domain, proportional to:

$$\tilde{T} \propto \tilde{G}(k_2/\cos \theta_t^R) \exp[(-\beta + jk_2 \tan \theta_t^R)x_1]. \quad (9)$$

The derivation of Eq. (9) with respect to  $x_1$  yields:

$$\Lambda_1 \propto |\tilde{\nabla T} \cdot \mathbf{x}_1|_{x_1=0} \propto \left| (-\beta + jk_2 \tan \theta_t^R) \tilde{G}\left(\frac{k_2}{\cos \theta_t^R}\right) \right|. \quad (10)$$

$\Lambda_1$  increases with  $k_2$  when the incidence is oblique, i.e.,  $\theta_t^R \neq 0$ , as long as the fall due to the Gaussian function  $\tilde{G}$  is

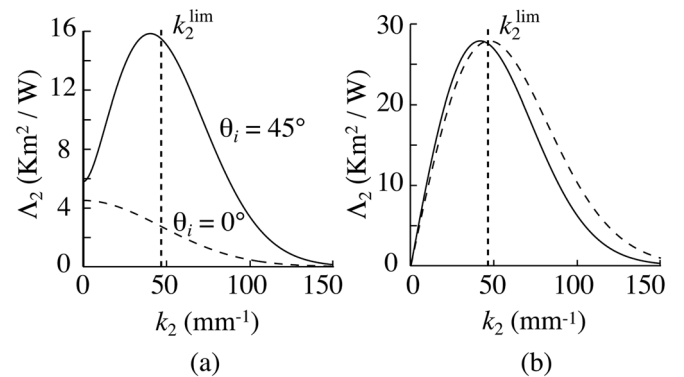


FIG. 2. Normalized projection of  $\tilde{\nabla T}$  on (a)  $x_1$  and (b)  $x_2$  vs.  $k_2$  for  $\theta_i = 0^\circ$  (dashed) and  $\theta_i = 45^\circ$  (solid) at  $\omega = \omega_c$  ( $\theta_i = 0^\circ$ ). The vertical line stands for  $k_2^{\text{lim}}$ .

not large enough to compensate the rise caused by  $k_2 \tan \theta_i^R$ . It appears in Fig. 2(b) that the maximum of  $\Lambda_2$  is shifted for oblique incidence configuration due to the term  $\cos \theta_i^R$  in the Gaussian function  $\tilde{G}$  [see Eq. (9)]. The derivation on  $x_2$  does not introduce additional dependency on  $\theta_i$  since it is a product by the quantity  $-jk_2$  in the Fourier domain. Thus a simple shift of the maximum is observed for  $\Lambda_2$  due to a change in the width of the Gaussian function  $\tilde{G}$ . At a given frequency, this result demonstrates that the magnitude of the source term of the wave equation is increased for  $k_2 \neq 0$ . Shear waves generation being related to wavenumbers  $k_2 \neq 0$ , shear waves generation should be enhanced when the incidence is oblique.

To localize the enhancement of shear-wave generation in the plane  $(\mathbf{x}_1, \mathbf{x}_2)$ , consider the following illustration. The volume source of expansion is reduced to a homogeneous infinite line of expansion corresponding to the refraction direction and the sample is considered as a half-space. In an infinite medium, this acoustic source would generate two plane compressional waves propagating normally to the direction of the line load with opposite directions. The wave propagating with a positive component  $k_2$  of the wavenumber along  $x_2$  is called the “propagating wave” and the wave propagating with a negative component  $k_2$  of the wavenumber along  $x_2$  is called “counter-propagating wave.” Since the medium is semi-infinite, the presence of the interface can lead to mode conversion. For positive values of the refractive angle, the counter-propagating wave is propagating away from the sample surface ( $k_1 > 0$ ) whereas the propagating wave is propagating towards the surface ( $k_1 < 0$ ). Thus the propagating wave can be mode-converted into shear waves upon reflection on the interface. So an enhancement of shear-wave amplitudes for  $x_2 > 0$  and a decrease for  $x_2 < 0$  is expected with respect to the situation where  $\theta_i = 0^\circ$ . The more the conversion from compressional to shear waves, the larger the fall in compressional-wave amplitude should be. The asymmetrical effect on the compressional-wave amplitude is therefore expected to be opposite to that on shear-wave amplitude.

### III. CALCULATIONS AND EXPERIMENTAL RESULTS

A Q-switched Nd:YAG (yttrium aluminum garnet) laser with a repetition rate of 50 Hz is focused on the front surface ( $x_1 = 0$ ) of a NG1 Schott glass sample. The relevant physical properties<sup>22,23</sup> of the sample are summarized in Table I. The laser delivers 20 mJ pulses of duration  $\sim 8$  ns. The fluctuation of laser light energy remains within 5%. A cylindrical lens of focal length 150 mm is used to form the laser line source.

A setup composed of moveable mirrors allows displacement of the source along the surface in a direction normal to the line source (Fig. 3). A motorized goniometer is used to control the incidence angle of the laser beam on the sample surface. The distance between the cylindrical lens and the sample is adjusted to ensure that the sample is positioned in the Rayleigh zone of the Gaussian beam.

A doubled CW Nd:YAG laser interferometer is focused to a point at the rear surface of the sample ( $x_1 = h$ ) to measure the normal component of surface displacements. Shear waves have a nonzero displacement component in the direc-

TABLE I. Mechanical, thermal and optical properties of Schott NG1 glass. The density  $\rho$  and the thickness  $h$  are measured. The stiffness coefficients  $C_{11} = \rho V_C^2$  and  $C_{66} = \rho V_S^2$  are calculated from the measured compressional-wave and shear-wave velocities:  $V_C$  and  $V_S$ , respectively.

	Value
Thickness (mm) $h$	1.36
Stiffness coefficient (GPa) $C_{11}$	66.91
Stiffness coefficient (GPa) $C_{66}$	23.24
Density (g/cm <sup>3</sup> ) $\rho$	2.44
Specific heat <sup>a</sup> (J/kg.K) $C_p$	840
Refractive index <sup>b</sup> $n$	1.51
Absorption coefficient <sup>b</sup> $\kappa$	$3.74 \times 10^{-4}$
Optical penetration depth <sup>b</sup> (mm) $\xi$	0.23
Thermal expansion <sup>b</sup> (K <sup>-1</sup> ) $\alpha$	$6.6 \times 10^{-6}$

<sup>a</sup>Reference 22.

<sup>b</sup>Reference 23.

tion normal to the plate surface<sup>7</sup> that can be measured by laser interferometry. The interferometer includes a band-pass filter operating between 20 kHz and 45 MHz. As shown in Fig. 3, the angle  $\theta_{\text{obs}}$  between axis  $\mathbf{x}_1$  and the source-receiver direction defines the observation angle.

The normal component of the acoustic displacement is measured for several  $\theta_{\text{obs}}$  with step  $\sim 2^\circ$  for both normal and  $\theta_i = 45^\circ$  incidences. The experimental signals are plotted with respect to time  $t$  and to source-receiver distance  $x_2$  (see Fig. 3) in Fig. 4. Signals are normalized with respect to the maximum amplitude measured for  $x_2 = 0$ . The black dotted line  $C$  indicates the arrival time of the compressional waves generated at the free surface, estimated from the sound velocity. The white dotted line  $S$  indicates the estimated arrival time of the shear waves, and the white dotted line  $3C$  indicates the estimated arrival time of the compressional echo reflected twice on the plate boundaries without mode-conversion. Arrows (1) and (2) point out asymmetric features detailed in the following.

In Fig. 5, the superimposition of experimental and calculated signals is presented for two symmetric positions of the receiver,  $x_2 = \pm 0.75$  mm (vertical dashed line in Fig. 4), for both configurations. The first compressional pulse  $C$  has a monopolar shape. The exponentially increasing part results from waves generated in the heated volume inside the sample and propagating toward the detection point. Reflection at the free surface without mode conversion yields the asymmetrical decrease of the compressive pulse. The compressive wave generated in this heated volume are also reflected with

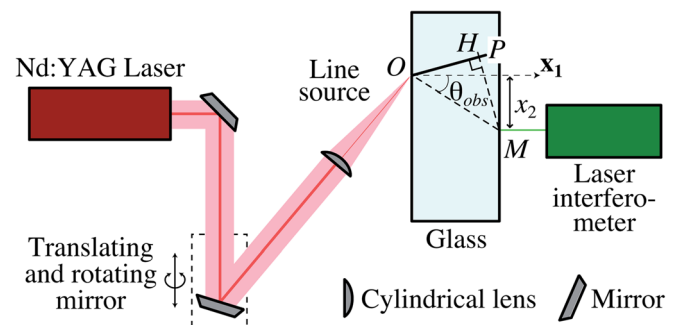


FIG. 3. (Color online) Experimental setup.

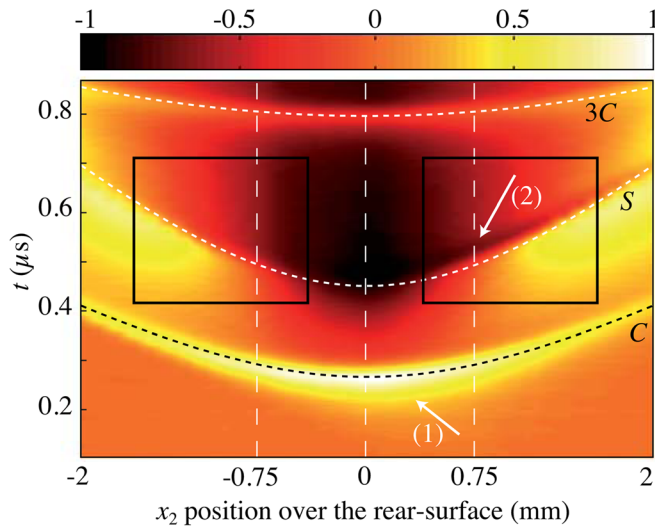


FIG. 4. (Color online) Normalized normal displacement measured at the rear-surface for  $\theta_i = 45^\circ$  vs. time and source-receiver position. The dotted lines labeled with  $C$ ,  $S$  and  $3C$  stand for the theoretical arrival time of compressional wave, shear wave and compressional echo reflected twice without mode-conversion, respectively. Arrows (1) and (2) point out asymmetrical behaviors. The black rectangles limit the zones where shear-wave amplitudes are extracted.

mode conversion at the free surface, giving rise to shear waves revealed by the first negative step  $S$  in the waveforms. Echoes result from successive reflections with or without mode conversion in the plate. Good agreement is observed between the simulation (dashed lines) and the experimental (solid lines) signals in terms of arrival time and shape. However, slight discrepancies between experimental and theoretical baselines appear because of the low-pass filtering by the laser interferometer.

Zoom-in on the first compressive pulse of each waveforms plotted in Fig. 5 are plotted in Fig. 6. Owing to symmetry, the first compressive pulse  $C$  retains the same shape for  $x_2 = -0.75$  mm and  $x_2 = 0.75$  mm for  $\theta_i = 0^\circ$ . However, the normal displacement at  $t = 0.2$   $\mu\text{s}$  (vertical dashed line in Fig. 6) clearly shows that the rise time of the  $C$  pulse differs for symmetric probe positions in the oblique incidence config-

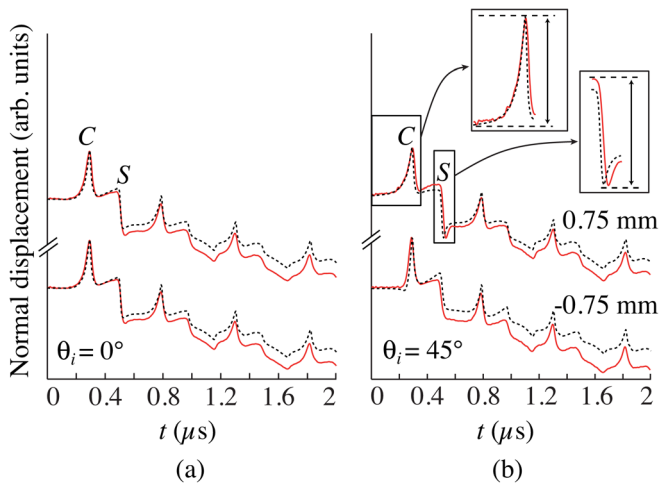


FIG. 5. (Color online) Experimental (solid) and simulated (dashed) normal displacement at two symmetric positions  $x_2 = -0.75$  mm (down) and  $x_2 = 0.75$  mm (up) on the rear surface of the plate for (a)  $\theta_i = 0^\circ$  and (b)  $\theta_i = 45^\circ$ . The insets in (b) show measurement of compressional-wave and shear-wave amplitude.

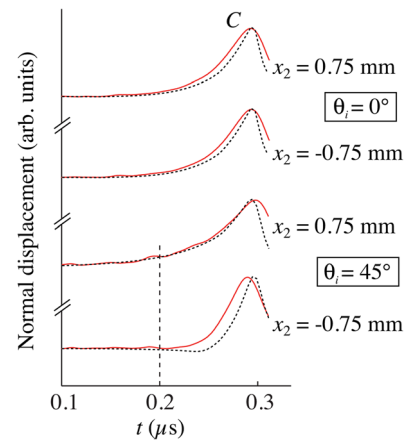


FIG. 6. (Color online) Zoom-in on the first compressive pulse for both positions  $x_2 = -0.75$  mm and  $x_2 = 0.75$  mm and both source orientations  $\theta_i = 0^\circ$  and  $\theta_i = 45^\circ$ .

uration. To analyze this striking feature, consider the penetrating acoustic source as a continuous sum of point sources of expansion distributed along the refracted direction, from the surface (point of expansion  $O$ , see Fig. 3) to a distance equal to the optical penetration depth  $\xi(\theta_r)$  (point of expansion  $P$ , see Fig. 3). The rise time  $\tau_C$  of the compressional waves is calculated as a function of  $x_2$ .  $\tau_C$  is defined as the difference between the times of flight of plane waves propagating from the point source the farthest to the observation point  $M$  and of plane waves propagating from the point source the nearest to  $M$ . The detailed expression of  $\tau_C$  is given in the appendix. Figure 7 shows the calculated rise time  $\tau_C$  versus  $x_2$  for normal and oblique configurations for the Schott NG1 glass sample. In both cases, the rise time on both sides of  $x_2 = 0$  tends to the same limit  $\tau_C^l = \xi(\theta_r) \sin \theta_r^R / V_C$  when the observation point is far enough from the source. The rise time is symmetric with respect to  $x_2 = 0$  for  $\theta_i = 0^\circ$ , whereas it is not symmetric any more in the oblique incidence case. The minimum rise time for  $\theta_i = 45^\circ$  corresponds to a position of the observation point  $M$  equidistant from  $O$  and  $P$ . The maximum rise time is reached when  $M$  belongs to the refraction direction ( $OP$ ),

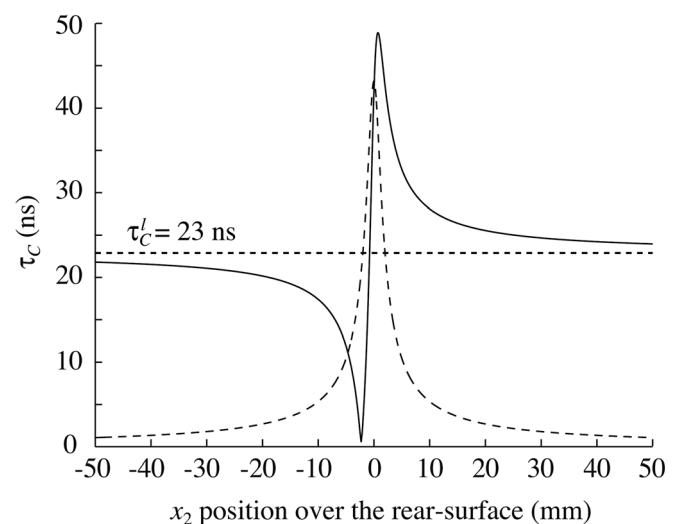


FIG. 7. Rise time of compressional waves vs. position at the rear surface of the plate for  $\theta_i = 0^\circ$  (dashed) and  $\theta_i = 45^\circ$  (solid). The horizontal line stands for  $\tau_C^l$ .

suggesting that the measurement of this maximum could provide a good approximation of the refraction angle. In the oblique incidence configuration, the rise time is larger for detection positions on the side where the source is refracted,  $x_2 > 0$  for  $\theta_i^R > 0$ . This explains the asymmetry in pulse  $C$  pointed out in Fig. 6, also shown by the arrow (1) in Fig. 4.

Compressional-wave and shear-wave amplitudes are measured from the waveforms as the differences between local maxima and minima (see insets in Fig. 5). The shear-wave amplitude at observation point  $x_2 = 0.75$  mm is larger than at observation point  $x_2 = -0.75$  mm for  $\theta_i = 45^\circ$ , whereas it is unchanged on both sides of  $x_2 = 0$  in the normal incidence case.

To further compare compressional-wave and shear-wave amplitudes on both sides of  $x_2 = 0$ , experimental and simulated normalized pulse amplitudes are plotted in Fig. 8 in polar coordinates with respect to the observation angle  $\theta_{\text{obs}}$  for both configurations. For each configuration, the signals are normalized by the compressional-wave amplitude for  $\theta_{\text{obs}} = 0^\circ$ . This normalization compensates for the loss in power density due to oblique optical transmission. For observation points close to  $x_2 = 0$ , both wave contributions are almost superimposed, the thickness of the sample being too small to provide sufficiently different times of flight. Moreover, since compressional waves are the fastest to reach farther observation points, shear waves  $S$  are competing with multiple reflections of the compressional waves with or without conversion ( $3C$  for example, see Fig. 4). Thus shear-wave amplitudes are measured only for observation points where no competition takes place. The corresponding zones of interest for the extraction of shear-wave amplitudes are shown in Fig. 4 with black rectangles. Although amplitude measurements are obtained for signals resulting from the normal displacement only, this representation can be thought as directivity patterns of the acoustic source for a half space.

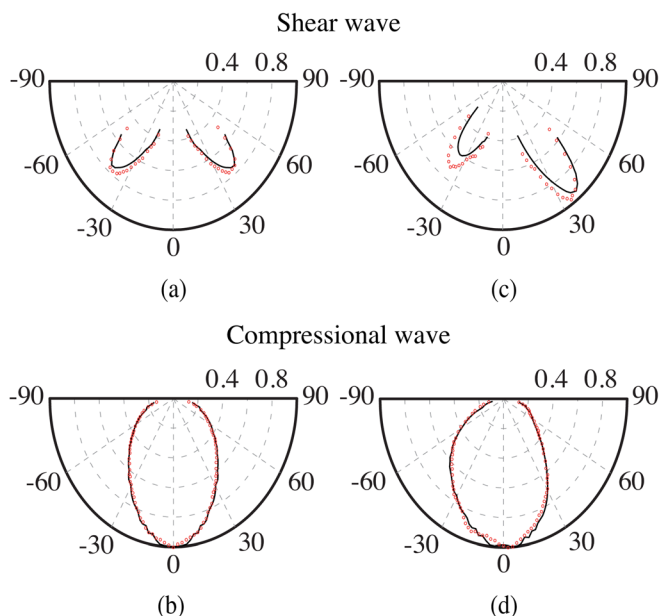


FIG. 8. (Color online) Amplitudes of (a) shear and (b) compressional waves for  $\theta_i = 0^\circ$  and amplitudes of (c) shear and (d) compressional waves for  $\theta_i = 45^\circ$  are plotted as a function of  $\theta_{\text{obs}}$  for both simulated (solid) and experimental (dots) results.

Good agreement between amplitudes calculated with experimental and simulated signals is observed and validates the chosen power density model [see Eq. (5)]. Slight differences between calculated shear-wave amplitudes and measured counterparts, appearing in Figs. 8(a) and 8(c), are probably due to the way amplitudes are extracted. The discrepancy is larger for the left lobe in Fig. 8(c) because of the weak generation of shear waves for  $\theta_{\text{obs}} < 0^\circ$  as previously pointed out for oblique incidence.

In Figs. 8(a) and 8(b), representing the normal incidence configuration, shear-wave and compressional-wave amplitudes are symmetric with respect to  $\theta_{\text{obs}} = 0^\circ$ . Previous studies<sup>24</sup> have demonstrated that the larger the source width is, the more directional the compressional waves are. The actual value of the source width  $a = 50$   $\mu\text{m}$ , a typical value in nano-second experiments, is determined by fitting experimental data with simulation results.

For  $\theta_i = 45^\circ$ , the value of  $a = 85$   $\mu\text{m}$  is also determined by fitting experimental data. The change with respect to the previous value of  $a$  is due to the oblique incidence of the laser beam. In Fig. 8(c), the loss of symmetry for  $\theta_i = 45^\circ$  is striking. As expected, amplitudes of shear waves generated by mode conversion upon oblique incidence are larger for  $\theta_{\text{obs}} > 0$  ( $x_2 > 0$ ) than for  $\theta_{\text{obs}} < 0$  ( $x_2 < 0$ ). In Fig. 8(d), the compressional-wave lobe is asymmetric. Amplitudes decrease for  $\theta_{\text{obs}} > 0$  and are enhanced for  $\theta_{\text{obs}} < 0$ . Thus, for  $\theta_i = 45^\circ$  the effect on the compressional-wave amplitudes is opposite to that on shear-wave amplitudes, as predicted previously.

#### IV. CONCLUSION

As shown by the calculations in Sec. II and confirmed by the experimental results, compressional and shear waves can be enhanced for oblique incidence of the laser source. The loss of symmetry of the acoustic source causes asymmetrical behavior of acoustic waves: shear-wave amplitude is increasing in the region where compressional-wave amplitude is decreasing and vice versa. Experimental and theoretical results promote the feasibility of the selection of specific bulk acoustic modes by tuning adequately the incidence angle of the source.

Following these results, fine measurements of the compressional-wave rise time for a set of source-receiver position should provide a good assessment of the refraction angle. Simultaneous measurement of the real part of the index of refraction and of acoustic properties of the material should be achieved. In addition performing such experiments on thinner plates or on less absorbing materials should help investigating a possible selection or enhancement of a specific Lamb mode, similarly to what can be achieved using transducer-based techniques.<sup>25</sup>

#### APPENDIX

The rise time of compressional waves is

$$\tau_C(x_2^{\text{obs}}) = \begin{cases} \frac{\max([OM], [MP]) - [MH]}{V_C}, & \text{if } x_2 \in [x_2^{\text{min}}, x_2^{\text{max}}], \\ \frac{|[MP] - [OM]|}{V_C}, & \text{if } x_2 \notin [x_2^{\text{min}}, x_2^{\text{max}}], \end{cases}$$

where  $O$ ,  $P$ , and  $H$  denote the point on the front-surface where the laser beam is focused, the point on the direction of refraction at a distance  $\xi$  from  $O$ , and the orthogonal projection of  $M$  on  $[OP]$ , respectively (see Fig. 3).  $V_C$  is the velocity of the compressional waves in the medium and the square brackets stand for distances between internal points. Boundaries  $x_2^{\min}$  and  $x_2^{\max}$  represent thresholds after which  $H$  no longer belongs to  $[OP]$ , i.e., positions of  $M$  where  $H$  and  $O$  are superimposed and where  $H$  and  $P$  are superimposed, respectively.

- <sup>1</sup>A. G. Bell, "Upon the production of sound by radiant energy," *Am. J. Sci.* **20**, 305 (1880).
- <sup>2</sup>T. H. Mainman, "Stimulated optical radiation in ruby," *Nature* **187**, 493–494 (1960).
- <sup>3</sup>R. E. Lee, and R. M. White, "Excitation of surface elastic waves by transient surface heating," *Appl. Phys. Lett.* **12**(1), 12–14 (1968).
- <sup>4</sup>S. J. Davies, C. Edwards, G. S. Taylor, and S. B. Palmer, "Laser-generated ultrasound: Its properties, mechanisms and multifarious applications," *J. Phys. D.* **26**(3), 329–348 (1993).
- <sup>5</sup>R. J. Dewhurst, D. A. Hutchins, S. B. Palmer, and C. B. Scruby, "Quantitative measurements of laser-generated acoustic waveforms," *J. Appl. Phys.* **53**(6), 4064–4071 (1982).
- <sup>6</sup>P. A. Doyle, "On epicentral waveforms for laser-generated ultrasound," *J. Phys. D.* **19**(9), 1613–1623 (1986).
- <sup>7</sup>L. R. F. Rose, "Point-source representation for laser-generated ultrasound," *J. Acoust. Soc. Am.* **75**(3), 723–732 (1984).
- <sup>8</sup>J. R. Bernstein, and J. B. Spicer, "Line source representation for laser-generated ultrasound in aluminum," *J. Acoust. Soc. Am.* **107**(3), 1352–1357 (2000).
- <sup>9</sup>I. Arias, and J. D. Achenbach, "Thermoelastic generation of ultrasound by line-focused laser irradiation," *Int. J. Solids Struct.* **40**(25), 6917–6935 (2003).
- <sup>10</sup>D. A. Hutchins, R. J. Dewhurst, and S. B. Palmer, "Directivity patterns of laser-generated ultrasound in aluminum," *J. Acoust. Soc. Am.* **70**(5), 1362–1369 (1981).
- <sup>11</sup>B. Castagnede, K. Y. Kim, W. Sachse, and M. O. Thompson, "Determination of the elastic constants of anisotropic materials using laser-generated ultrasonic signals," *J. Appl. Phys.* **70**(1), 150–157 (1991).
- <sup>12</sup>H. Sontag, and A. C. Tam, "Optical monitoring of photoacoustic pulse propagation in silicon wafers," *Appl. Phys. Lett.* **46**(8), 725–727 (1985).
- <sup>13</sup>A. Mourad, M. Deschamps, and B. Castagnede, "Acoustic waves generated by a transient line source in an anisotropic half-space," *Acustica* **82**(6), 839–851 (1996).
- <sup>14</sup>B. Audoin, and S. Guilbaud, "Acoustic waves generated by a line source in a viscoelastic anisotropic medium," *Appl. Phys. Lett.* **72**(7), 774–776 (1998).
- <sup>15</sup>C. Rossignol, J.-M. Rampoux, M. Perton, B. Audoin, and S. Dilhaire, "Generation and detection of shear acoustic waves in metal submicrometric films with ultrashort laser pulses," *Phys. Rev. Lett.* **94**(16), 166106 (2005).
- <sup>16</sup>V. Gusev, "On generation of picosecond inhomogeneous shear strain fronts by laser-induced gratings," *Appl. Phys. Lett.* **94**(16), 164105 (2009).
- <sup>17</sup>D. H. Hurley, O. B. Wright, O. Matsuda, V. E. Gusev, and O. V. Kolosov, "Laser picosecond acoustics in isotropic and anisotropic materials," *Ultrasonics* **38**, 470–474 (2000).
- <sup>18</sup>T. Pezeril, N. Chigarev, P. Ruello, S. Gougeon, D. Mounier, J.-M. Breteau, P. Picart, and V. Gusev, "Laser acoustics with picosecond collimated shear strain beams in single crystals and polycrystalline materials," *Phys. Rev. B* **73**(13), 132301 (2006).
- <sup>19</sup>A. C. Tam, "Pulsed-laser generation of ultrashort acoustic pulses: Application for thin-film ultrasonic measurements," *Appl. Phys. Lett.* **45**(5), 510–512 (1984).
- <sup>20</sup>B. Audoin, H. Meri, and C. Rossignol, "Two-dimensional diffraction of plasma, thermal, and elastic waves generated by an infrared laser pulse in semiconductors," *Phys. Rev. B* **74**(21), 214304 (2006).
- <sup>21</sup>Y. Wang, Y. Liu, J. Xu, H. Zhang, L. Bai, Y. Xiao, J. Yan, and X. Zhang, "Numerical study of lateral displacements of Gaussian beams reflected from weakly absorbing media near the Brewster dip and reflected from strongly absorbing media," *J. Opt. A: Pure Appl. Opt.* **11**(10), 105701 (2009).
- <sup>22</sup>P. A. Tipler, *Physics for Scientists and Engineers*, fifth edition (W.H. Freeman, New York, 1999), p. 560.
- <sup>23</sup>Schott datasheet on Neutral density NG1 glass (2008), [http://www.schott.com/advanced\\_optics/english/download/schott\\_neutral\\_density\\_ng1\\_2008\\_e.pdf?PHPSESSID=689rd0344ec6ntb7nfhcpunt21](http://www.schott.com/advanced_optics/english/download/schott_neutral_density_ng1_2008_e.pdf?PHPSESSID=689rd0344ec6ntb7nfhcpunt21)
- <sup>24</sup>B. Yuhai, P. Liwei, F. Qiping, Y. Yuping, and Y. Chongfu, "Experimental studies of directivity patterns of laser ultrasound in neutral glasses," *Ultrasonics* **33**(6), 429–436 (1995).
- <sup>25</sup>J. J. Ditri and K. Rajana, "An experimental study of the angular dependence of Lamb wave excitation amplitudes," *J. Sound Vib.* **204**(5), 755–768 (1997).